Investigation of strain localization in sheared granular layers using 3-D discrete element modeling

Chien-Cheng Hung [a,*], André R. Niemeijer [a], Amir Raoof [a], Thomas Sweijen [b]

[a] *Department of Geoscience, Utrecht University, Utrecht, the Netherlands*
[b] *Crux Engineering BV, Amsterdam, the Netherlands*

ARTICLE INFO

ABSTRACT

In this work, we investigate slip localization in sheared granular faults at seismic velocities using 3-D numerical simulations with the discrete element method (DEM). An aggregate of non-destructive spherical particles is subjected to direct shear by using two moving boundaries in a sandwich configuration to identify the impact of particle-scale parameters on slip localization. We impose a thin layer of fine-grained particles with variable contrast in thickness and grain size adjacent to the boundary as well as in the middle of the granular layer to simulate boundary and Y shears observed in both natural and laboratory fault gouges. The results show that larger amounts of strain is accommodated within the pre-described finer-grained layer even with a small ($<10\%$) contrast in grain size. Up to 90% of the displacement is localized in a finer-grained layer when the contrast ratio of the grain size is 50%. Based on the concept of the average spreading velocity of particles and squeeze expulsion theory in granular flow, we suggest that the phenomenon of localization is likely from result from the contribution of larger grains collisions with smaller grains. Since the amount of frictional heat generated depends on the degree of localization, the results provide crucial information on the heat generation and associated slip accommodation in sheared gouge zones. We conclude that the occurrence of a weaker, fine-grained layer within a dense fault zone is likely to result in self-enhanced weakening of the fault planes.

1. Introduction

Field and borehole observations of active seismogenic fault zones show that earthquake slip is often focused within a gouge-bearing slip zone of a few centimeters thick surrounded by damage zones of cataclasite with or without foliation and fractured country rock (Chester et al., 1993; Chester and Chester, 1998; Heermance et al., 2008; Boullier et al., 2009; Boullier, 2011). Microstructural studies further demonstrate that most of the slip occurs within a fine-grained principal slip zone (PSZ) cut with discrete sliding surface or multiple surfaces with a thickness less than a few hundreds of microns (Chester and Chester, 1998; De Paola et al., 2008; Boullier et al., 2009; Heesakkers et al., 2011; Smith et al., 2011; Fondriest et al., 2012). Laboratory friction experiments performed on granular fault materials at seismic slip velocity, like 1 m/s, have demonstrated the reproducibility of such an extreme localization of shear zones (with a thickness $< \sim 100$ μm) commonly characterized by grain size reduction, which are defined as boundary or Y shears (Han et al., 2010; Kitajima et al., 2010; De Paola et al., 2011; Fondriest et al., 2013; Smith et al., 2013, 2015; Yao et al., 2013; Kuo

et al., 2014).

Smith et al. (2015) experimentally investigated the dependency of the mechanical behavior on strain localization by shearing calcite gouges at seismic slip velocity for meters displacement and found that the formation of a localized high-strain shear band (i.e., PSZ) may play a critical role in the dynamic weakening of a fault. Once the PSZ has formed, it accommodated subsequent deformation and more shear heating and thus faster weakening would occur. Based on numerical simulations Platt et al. (2015) showed that the thickness of the PSZ has great influence on various earthquake parameters. For a fault-zone gouge in which thermal decomposition and thermal pressurization are active, they showed that a decrease in PSZ thickness leads to faster rupture velocity and shorter total slip of an earthquake. Thus, understanding of strain localization and the distribution of earthquake slip within a gouge-filled fault zone is critical to constrain local heat production, temperature rise and weakening; hence, the fault behavior and associated earthquake physics. Localization of strain at nucleation velocities and small displacement as well as at seismic velocities and large displacements has been studied in laboratory experiment (e.g., Logan

et al., 1992; Smith et al., 2015) and numerical simulation (e.g., Mair and Hazzard, 2007; Casas et al., 2022). However, slip localization has not been investigated so far for seismic velocity and small displacements (i. e., few centimeters) which is important for induced seismicity.

Numerical discrete element modeling (DEM) has been widely used to study the deformation of granular materials. Using DEM, we can investigate dynamic microscale processes of shear zones as they deform and evolve. Morgan and Boettcher (1999) conducted 2-D numerical simulations of homogeneous sheared granular gouge by varying both particle size distributions (PSD) and interparticle friction at subseismic slip rates of 0.1 mm/s). They showed that both an increasing number of fine grains and a larger value of interparticle friction favor transient localization of strain. They interpreted this to be the result of an increased importance of interparticle rolling in accommodating granular deformation. Mair and Hazzard (2007) used DEM to investigate homogeneous sheared granular materials in 3-D in which out-of-plane deformation is considered and found that contact force networks are sensitive to PSD. Despite observing changes in the network of grains that support the bulk of the force with changes in PSD, they do not report discernible persistent localized deformation in the granular layer.

In natural fault zones, grain fragmentation and time-dependent processes such as contact healing are important mechanisms operating during both aseismic and coseismic slip. On the basis of 2-D DEM simulations at subseismic velocities, Morgan (2004) reported that shear strain tends to localize within a boundary-parallel shear band (1 to ~10 grains thick depending on the imposed sliding velocity) when time-dependent contact healing is introduced. Mair and Abe (2008) used a particle-based 3-D DEM model with breakable bonds to simulate grain fracturing process during fault gouge evolution and revealed that in their simulations strain localization is strongly correlated to enhanced grain size reduction. A recent 2-D numerical study of cemented granular fault gouge by Casas et al. (2022) reported that interparticle bond (i.e., cohesion) plays a key role in influencing slip weakening and gouge deformation at seismic velocity. A gouge layer with high cohesion (>95%) is prone to generate large weakening and develop localized deformation such as R and Y shears owing to its relatively small (<1%) critical dilation (i.e., necessary dilation for macroscopic shear failure).

In the absence of the above-mentioned time-dependent processes at grain contacts, Zhu et al. (2018) performed 2-D interface shear simulations at medium slip velocity (few mm/s) and showed evident features of slip localization similar to boundary shear. They reported that a localized shear band would occur at an early stage of sliding (i.e., strain hardening phase) in both loose and dense granular layers and the degree of localization has a strong correlation with shear stress. Ferdowsi and Rubin (2020) studied sliding from subseismic (10^{-5} m/s) to coseismic (1 m/s) velocity using 3-D simulations of velocity-steps where momentum transfer was suggested to be the only time-dependent process; however, no sign of persistent localized deformation was observed shortly after an increase in velocity. They suggested that formation of localized deformation may be characterized using different values of dimensionless parameters such as inertial number, I, or dimensionless pressure, P. (Ma et al., 2020).

Based on the previous numerical studies, it is clear that slip localization would occur within a numerical homogeneous sheared gouge zone at a wide range of slip velocity (subseismic to seismic) if a time-dependent process is considered. Without considering time-dependent processes, whether persistent localization deformation would occur may depend on various input parameters, such as sample dimension, slip velocity, and grain size distribution. In this study, we focus on 3-D gouge deformation sheared at seismic slip rate (1 m/s) for short displacement (up to 20 mm) within a non-breakable gouge assemblage. We systematically investigated slip distribution within a granular assemblage with an existing fine-grained layer parallel to the shear direction as shear strain is often reported to localize within a thin shear band with finer grain size. We then quantified how much slip occurs within the localized shear band if localization occurs to see how much localized grain size

reduction (producing fine-grained layers with variable thicknesses) is required to induce localization. Final, we provide insight into the physical mechanism of strain localization, the link between natural and experimental observations on mechanical behavior, as well as the role of fine-grained particles in fault dynamics.

2. Methods

2.1. Discrete element method

The discrete element method (DEM) is widely used to investigate the mechanics of granular materials. In this technique, individual particles are considered as discrete elements, or grains, which interact with each other at their contact points. An explicit numerical scheme is applied to solve the translational and rotational equations of motion for every particle, given as, respectively:

$$\vec{F}_i = m_i \ddot{\vec{x}}_i \tag{1}$$

$$\vec{M}_i = I_i \dot{\vec{\omega}}_i \tag{2}$$

where $\vec{F}_i$ and $\vec{M}_i$ are the net force and moment of particle i, m_i and I_i the mass and moment of inertia, and $\ddot{\vec{x}}_i$ and $\dot{\vec{\omega}}_i$ the linear and angular acceleration, respectively. Vectors $\vec{F}_i$ and $\vec{M}_i$ are updated each time step and are obtained from the sum of the corresponding network of contact forces $\vec{F}_{ij}$ applied on each particle i with its neighboring particles j. Contact forces $\vec{F}_{ij}$ are computed from a given force-displacement relationship (see Eqs. 5 and 6).

The time step used in this study is constrained by the amount of time that an elastic wave takes to propagate within a given particle of a specific size. Assuming Young's modulus and density of particles have continuum-like quantities, the critical time step can be written as:

$$\Delta t_{cr} = \min_i \left[R_i \sqrt{\frac{\rho_i}{E_i}} \right] \tag{3}$$

where R_i is the particle radius, ρ_i the particle density, and E_i the Young's modulus. A safety factor of 0.3 is used in Eq. (3) which satisfies the critical time step calculated from the minimum eigenvalue of a system of interacting particles, given as:

$$\Delta t_{cr} = \sqrt{\frac{m_i}{K}} \tag{4}$$

where K is an estimated equivalent contact stiffness (Itasca, 1999). The resulting time step in the range $\sim 10^{-8}$ to $\sim 10^{-9}$ s, depending on the grain size, produces both stable and accurate numerical simulation. For more details on the implementation of the methods, see the documentation of the DEM open-source code in Yade (Šmilauer et al., 2010).

Here we use the DEM to simulate direct shear of a granular layer with an assembly of spherical particles in 3-D. All the spherical particles are indestructible and prescribed by specific micro-properties (Table 1).

Table 1
DEM simulation parameters and coefficient values.

Numerical setup parameter	Value	Particle parameter	Value
Sample dimension (length × width × height)	10 × 3.75 × 3.75 (mm)	Density, ρ	2500 (kg/m²)
Normal stress, σ_n	**5**, 20, 40 (MPa)	Young's modulus, E	55 (GPa)
Slip velocity, V	**1**, 0.1 (m/s)	Poisson ratio, λ	0.25
Mean particle diameter, d	250 (μm)	Viscous damping	0.3
		Rolling friction coefficient, η	**0**, 0.5

Note. The values with bold font refer to reference model value.

Particle-particle interactions follow the Hertz-Mindlin (HM) contact model with no micro-slip solution (Mindlin, 1949) which is appropriate for elastic contact bodies (Thornton et al., 2011). In the HM model, the normal force-displacement and shear force-displacement relationships are expressed as:

$$F_n = \frac{4}{3} E^* R^{*1/2} u_n^{3/2} \tag{5}$$

$$F_s = 8 a G^* u_s \tag{6}$$

where u_n and u_s are the normal and shear displacement between particles, a is the contact radius, E^*, R^*, and G^* are the equivalent elastic modulus, equivalent radius, and equivalent shear modulus, respectively, which are given by:

$$\frac{1}{E^*} = \frac{1 - v_1^2}{E_1} + \frac{1 - v_2^2}{E_2} \tag{7}$$

$$\frac{1}{R^*} = \frac{1}{R_1} + \frac{1}{R_2} \tag{8}$$

$$\frac{1}{G^*} = \frac{2 - v_1^2}{G_1} + \frac{2 - v_2^2}{G_2} \tag{9}$$

where v_1 and v_2 are the Poisson's ratios of the two conforming bodies. The normal and shear stiffness, k_n and k_s can then be written as

$$k_n = 2 E^* \sqrt{R^* u_n} \tag{10}$$

$$k_s = 8 G^* \sqrt{R^* u_n} \tag{11}$$

The shear force F_s at each grain contact is limited according to the Mohr-Coulomb failure criterion which follows from the coefficient of interparticle friction assuming zero cohesion. Once the shear force is overcome, two particles will slide relative to each other at their contact point.

Aside from interparticle sliding, interparticle rolling is also introduced in the model, particularly owing to the use of spherical particles. To investigate the relative importance of rolling and sliding in our simulations, we add rolling resistance to the particle interactions. The rolling resistance model adopted in this study was implemented in Yade by Modenese (2013). In the model, we firstly define the torsional rotation $\vec{\theta}_t$, and the rolling rotation $\vec{\theta}_r$ from the total relative rotation $\vec{\theta}$ of two contacting particles as:

$$\vec{\theta}_t = \left(\vec{\theta}_t \bullet \vec{n} \right) \vec{n} \tag{12}$$

$$\vec{\theta}_r = \left(\vec{\theta} \bullet \vec{n} \right) \vec{n} \tag{13}$$

where $\vec{n}$ is the unit vector defining the normal to the contact. The torsional moment is disregarded while the bending moment is finally computed as:

$$\vec{M}_r = k_r \vec{\theta}_r = \beta k_s R^{*2} \vec{\theta}_r \tag{14}$$

where β is a dimensionless parameter which is set to be 1, k_r and k_s the rolling stiffness and shear stiffness, respectively, and R^* the equivalent particle radius. The maximum rolling moment that can be exchanged between two particles is then limited by the normal contact force, F_n, in a form equivalent to the MC criterion, according to:

$$M_r \leq M_{max} = |F_n| R^* \eta \tag{15}$$

where η is the coefficient of rolling friction. Therefore, we can set the interparticle rolling resistance by defining k_r and η. In the present study, we determine k_r as 1.75×10^{-3} by following Eq. (14) for all the simulations where k_s and R^* are 4.5×10^5 N/m and 6.25×10^{-5} m,

respectively (e.g., Iwashita and Oda, 1998).

2.2. Design of numerical experiments

2.2.1. Gouge sample configurations

The numerical simulation represents a direct shear experiment of a particle packing having a layered, sandwiched structure. The simulation consists of top and bottom frictionless walls, top and bottom boundary granular layers, and a main granular layer (Fig. 1). Top and bottom frictionless walls are used to confine particles in the vertical direction (i.e., y-coordinate) and top and bottom controlled granular boundary layers are used to provide roughness to the interface with the gouge layer. Such top and bottom boundary layers were randomly generated without a perfect ordering of grains to simulate a random surface roughness. We apply periodic boundary conditions in the horizontal direction (i.e., x and z-coordinate) so that particles exiting from one side reappear from the opposite face. No walls are applied to confine the front, back, left, and right side of the assemblage. The size of the main granular layer is $40d$ (length) $\times$ $15d$ (height) $\times$ $15d$ (width) in the x, y, and z direction, respectively, where d is the mean particle diameter of 250 μm.

In this study, we use a principal slip zone (PSZ) model, referring to a granular packing with a single-size PSD with an additional layer of particles with a single-size PSD with a finer grain size (Fig. 1). The fine-grained layer is parallel to the shear direction within the main granular layer to mimic the presence of a Y or boundary shear due to localized grain size reduction. With this model, we explore how much contrast in grain size and thickness of the PSZ is required for slip to be fully accommodated within the PSZ by changing its grain size and thickness while maintaining the same total thickness of the layer. This results in the change of the total number of particles within the granular assemblage. We choose four different particle sizes of the finer grain layer ($0.9d$, $0.75d$, $0.6d$, and $0.5d$) and five different thicknesses of the PSZ ($1/8\,t$, $1/4\,t$, $3/8\,t$, and $1/2\,t$ where t is the thickness of the gouge layer with a value of 3.75 mm without controlled boundary layers). For comparison, we additionally use a homogeneous model which is a randomly distributed granular assemblage with a uniform grain size distribution without any additional layers of particles. With this model, we generate a particle packing with a narrow to a wide particle size distribution (PSD) and create random spatial variations in grain size (see Fig. S1 for more detail).

The chosen particle population and sizes with the top and bottom controlled boundary layers provide a total sample thickness h of $\sim$4 mm, normal stress σ of 5 MPa, slip velocity V of 1 m/s, interparticle friction μ of 0.5, with viscous damping of 0.3, and no interparticle rolling resistance (free rolling) as the reference settings. We select $0.5d$ and $1/8\,t$ as
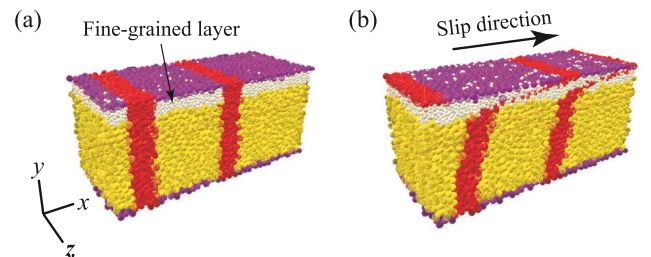
Fig. 1. The principal slip zone (PSZ) model with a $0.5d$ and $1/8\,t$ fine-grained layer (shown in white) parallel to the slip direction. (a) Conditions before shearing, and (b) after shearing with to a total shear strain of 100%. The boundary layer particles are shown in purple. Two vertical layers of grains are colored red to serve as strain markers. Fully homogeneous deformation would result in a rotation of the vertical boundaries of these layers to an angle of 45° at a final shear strain of 100%. The top and bottom frictionless walls are not shown. (For interpretation of the references to color in this figure legend, the reader is referred to the web version of this article.)

the reference contrast in grain size and layer thickness, respectively. The values of these parameters are chosen to be comparable to previous DEM numerical simulations while applying a slip velocity appropriate for granular shearing at seismic velocity (Morgan, 1999; Hazzard and Mair, 2003; Mair and Hazzard, 2007). The shear velocity is high and yields a shear strain rate $\dot{\gamma}$ of 266, defined as the ratio of shear velocity (1 m/s) to the undeformed sample height (3.75 mm). Such a high strain rate yields an inertial number $I = \dot{\gamma}\overline{d}/\sqrt{\sigma/\rho} \approx 1.5 \times 10^{-3}$, which put our simulations just in the dense flow regime ($10^{-3} < I \langle 10^{-1}$) (Ferdowsi and Rubin, 2020; Ma et al., 2020). In fact, the I value remains similar in all simulations for our applied input parameters.

2.2.2. Numerical setup for direct shear simulations

The sample is sheared to a maximum of 500% shear strain, defined as $\gamma = dx/h$, where x and h are the instantaneous displacement in the shear direction and the instantaneous sample thickness, respectively. Note that the actual shear strain of the gouge layer is ~10% larger than the imposed value as the thickness of the actual gouge layer t accounts for ~90% of the total sample thickness h, In the following, we use the imposed value (500%) for the results.

We apply the following procedure to perform simulations for direct shear:

1. Generate a loose granular assemblage in a cell in which particles with the assigned micro-properties are randomly distributed.
2. Apply isotropic compression to the cell until a cell pressure of 10 kPa is reached to achieve a dense granular packing.
3. Apply normal stress vertically to the top frictionless wall. To maintain the desired normal stress, a servo-control mechanism which adjusts vertical (z direction) wall velocity throughout the experiment is applied.
4. Impose a velocity with a progressive acceleration ramp to the top boundary layer in the positive x direction to apply shear to the granular layer. During shearing, top boundary particles are made to move only in the vertical motion (xy-plane) while at the bottom boundary particles are fixed.

During the shearing, we continuously monitor the particle-scale properties, such as particle motion, as well as macroscopic properties, such as friction and gouge volume (dilation). Particle motion parameters like, particle displacement, linear velocities, and rotations are measured to observe dynamics of particle interactions. For example, using a Gaussian weight function, we can define the particle displacement at a specific height y as the weighted averages of the displacement in the x direction associated with the particles present at (or near) this height.

The Gaussian weight function has a form of: $\Omega(x) = e^{\left(-\frac{(x-\mu)^2}{2\sigma^2}\right)}$, where x is the specific sample height, μ is the location of the center, and σ determines the width of the bell curve. This information provides profiles of particle displacement as a function of sample height to visualize the deformation of the 3D sheared granular layer. The macroscopic friction coefficient of the granular system is obtained by calculating the ratio of the sum of the shear force acting on the top (which drives boundary particles) to the applied normal load (i.e., shear stress divided by normal stress). The volumetric behavior of the gouge layer is a macroscopic reflection of dynamic particle motions associated with interparticle sliding and rolling.

3. Results

3.1. Macroscopic behavior

Fig. 2 shows the macroscopic behavior of the granular assemblages, including macroscopic friction, dilatancy rate, and volumetric strain for the PSZ reference model with different seed conditions (i.e., different realizations). For the dilatancy rate and volumetric strain, we monitor
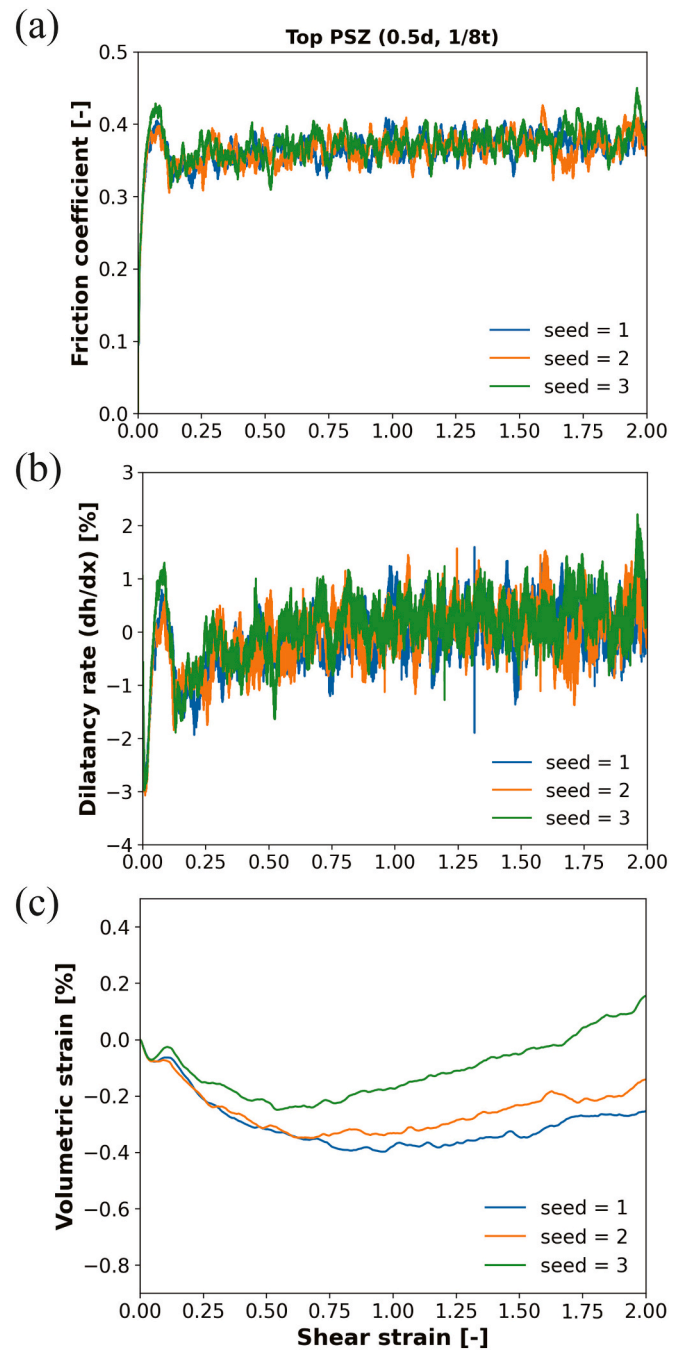
Fig. 2. Evolution of the macroscopic friction, dilatancy rate (dh/dx), and volumetric strain ((h-h_0)/h_0) as a function of shear strain up to 200% shear strain for the simulations of the top PSZ model with $0.5d$ and $1/8$ t. A positive change in dilatancy rate and volumetric strain indicates dilation and a negative change shows compaction. The gray dashed lines indicate a positive correlation between the friction and the dilatancy rate.

the change of the vertical displacement of the top wall to measure the volume of the system throughout shearing, expressed as an dilatancy rate, dh/dx, as well as volumetric strain, ($h-h_0$)/h, respectively. Note that positive values indicate dilation and negative values indicate compaction. In general, our PSZ model have good reproducibility in macroscopic behavior as a function of shear strain. For the macroscopic friction, a peak friction of about 0.4 was first achieved followed by a sharp friction drop to approximately 0.32 within 10% of shear strain. With increasing shear strain, quasi-steady-state friction (~0.37) was attained. A positive correlation between friction and dilatancy rate can

be observed. For the volumetric strain data, during initial shearing, all granular systems show instantaneous compaction followed by dilation. With increasing shear strain, the gouge layer begins to compact once more until 50–70% of the shear strain depending on the seed conditions, followed by continuous dilatation. The non-constant level of the volumetric strain at 200% shear strain may suggest the mixing of the fine- and coarse-grained layer.

3.2. Particle displacement

We divide the shear zone (thickness of ~4 mm including controlled boundary layers) into 100 sub-layers and obtain the weight averaged particle displacement for each region (in the y direction) of the sublayer. In averaging, the relatively fine (e.g., 100 division) or relatively course (e.g., 64 division) resolution of the division did not influence the particle displacement curve. Fig. 3 shows the particle displacement plot of the PSZ model with 0.5d and 1/8 t with different seed conditions. The gray dashed line indicates the interface between the fine- and coarse-grained layers (FCG). The results not only show good reproducibility but also illustrate qualitative consistency with the visual deformation of the boundaries of the marker band in the 3-D model (Fig. 1). For most of the PSZ model, the displacement curve displays a critical point roughly at the interface between the fine- and coarse-grained layers, defined as FCG interface afterwards. Such a pattern demonstrates that most of the slip is accommodated within the fine-grained layer and little strain is accommodated in the coarse-grained layer (<10% of the total strain).

3.2.1. Influence of PSZ parameters: Grain size and layer thickness effects

In Fig. 4, we compare the results of the PSZ model with different contrasts in grain sizes and thicknesses of the fine-grained layer. The FCG interface is kept at the same height in all shearing simulations. For most simulations, the results show that the particle displacement significantly increases from the bottom to the top when passing through the FCG interface and a clear change of slope in displacement can be observed. This demonstrates that most of the slip is accommodated within the fine-grained layer and not much strain occurs outside of it. In addition, the amount of slip that occurs outside of the PSZ decreases with increasing contrast in grain size and PSZ thickness. Note that there is no clear critical point in all simulations with a grain size contrast of 0.9d and the displacement curve is similar to the one with the single-size PSD (Fig. 4a). We observe that the localization pattern within the fine-grained layer can be varied between different thickness contrast
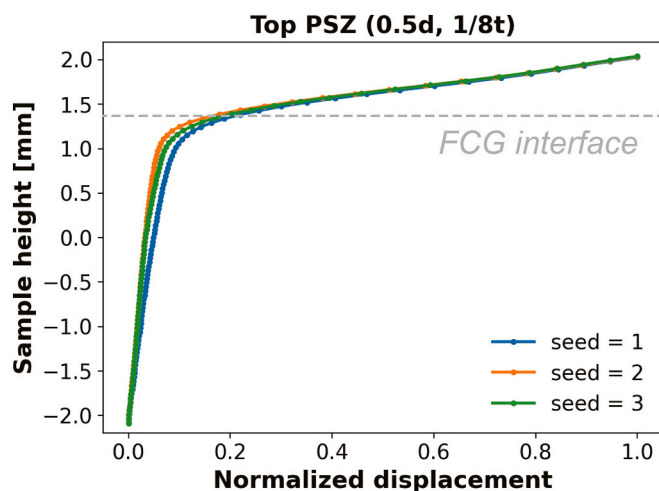
ratios, specifically for 0.5d grain size contrast. The pattern evolves from a straight line to a upward curved line with increasing thickness contrast which indicates that more slip is localized near the FCG interface.

3.2.2. Influence of location of PSZ on deformation pattern

To see the influence of the location of the PSZ on the shear deformation and further analyze to what extent slip localization operates in the model configuration of 0.9d and 1/8 t, we run additional simulations where a fine-grained layer is imposed at the middle and bottom of the granular layer. In Fig. 5, we compare the displacement curves for the top, middle, and bottom boundary PSZ models with 0.9d and 1/8 t as well as 0.5d and 1/8 t at about 500% shear strain. For the simulation with 0.9d (Fig. 5a), the results shows that the displacement curves of the top and bottom PSZ have opposite patterns where for the bottom PSZ boundary simulation, most of the deformation is accumulated at the bottom region. On the other hand, the simulation with a middle PSZ shows nearly linear deformation. By comparison with the simulation using a single-size, localized deformation is hardly affected by the presence of a PSZ at the top boundary. When the contrast in grain size is larger (0.5d in Fig. 5b), we can clearly identify the critical point of the displacement curves, regardless of the location of the PSZ, suggesting that a larger amount of slip is localized within the PSZ.

3.2.3. Influence of shear strain on deformation pattern

Fig. 6a shows the normalized particle displacement for the top PSZ model with 0.5d and 1/8 t with shear strain from 10%, roughly the state of peak friction for all models, up to 500%, the maximum shear strain imposed in laboratory direct shear experiments (e.g., Hunfeld et al., 2017). For the 1/8 thickness ratio, we show that an increasing localization of slip until 100% shear strain is reached. The degree of localization does not change further from 100% to 500% shear strain. We find that slip is already localized at the peak friction. To further investigate the location and the instance of the localization, we look at the top PSZ model with 0.5d and 1/2 t with shear strain starting from 1%, at strain-hardening state, to up to a value of 50%. We find that the gouge deformation begins to exhibit visible localization between the shear strain of 1% and 5%. The deformation pattern changes from a nearly linear curve at 1% to a non-linear curve at 5%, indicating that the initial slip is localized at the FCG interface as well as the boundary between the top boundary layer and the fine-grained layer. With increasing shear strain, slip is more localized within the fine-grained layer and specifically accumulates near the boundary with significant contrast in grain size (red rectangle region).

3.2.4. Influence of interparticle friction and rolling resistance on deformation pattern

Fig. 7a–c shows the results of the deformation patterns with varied interparticle friction μ and rolling friction η for PSZ models with different contrast in grain size and PSZ thickness. We find that an increase in μ leads to a more localized deformation whereas the simulation with lower μ have a boarder deformation zone. In addition, the simulation with η of 0.5 becomes indistinguishable in the simulations with the power-law PSD (Fig. 7c).

To explore whether the low interparticle friction of the fine-grained layer itself could induce further slip localization, we performed simulations using the PSZ model with 0.9d and varied layer thicknesses (1/8 t and 1/2 t), but only decreasing the μ of the fine-grained layer. Fig. 7b and c show that slip becomes more localized within the fine-grained layer with decreasing μ_{PSZ}, regardless of PSZ thickness.

3.3. Porosity profile

Fig. 8 shows assemblage porosity along the sample height for numerical models with different contrasts in PSZ thicknesses and grain sizes as well as the location of the PSZ. Calculation of the porosity is based on the triangulation of the spheres, in which the particle-centered

Fig. 3. Normalized particle displacement (Δx/max(x)) along the height of sample for the top PSZ model with 0.5d and 1/8 t using different seed conditions. The gray dash line indicates the initial fine- and coarse-grained interface (FCG interface).
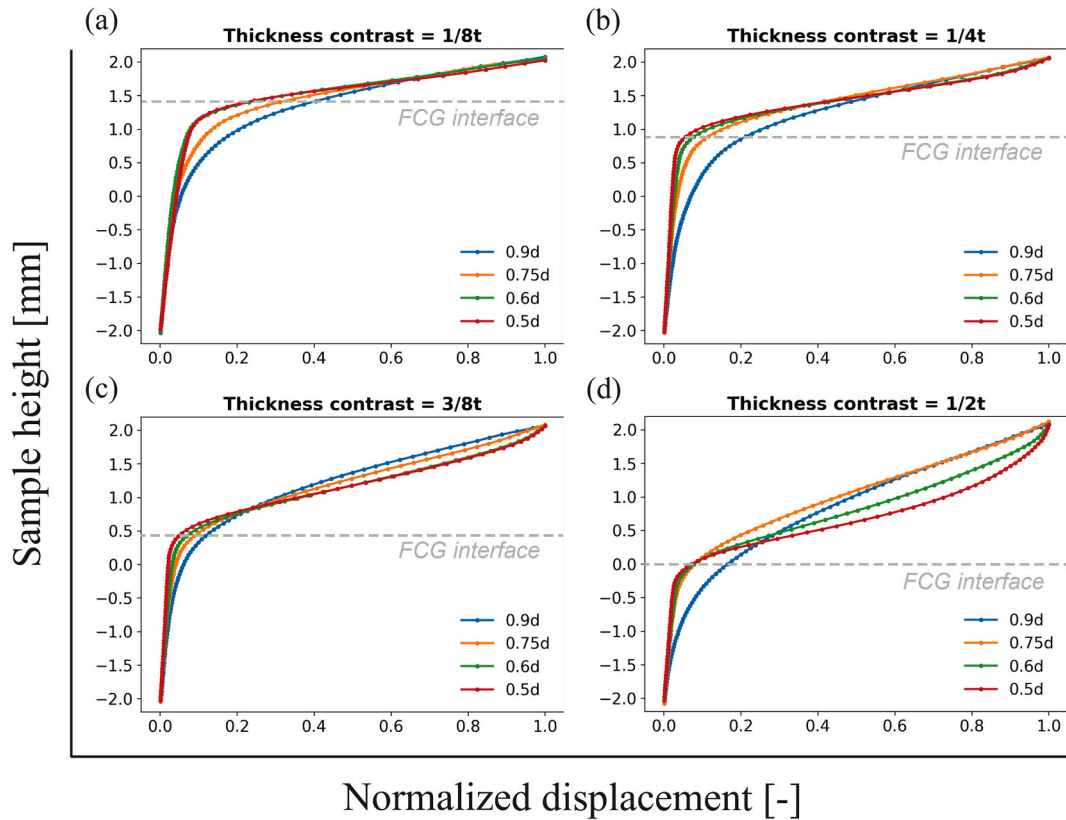
Fig. 4. Normalized particle displacement along the height of sample for all grain size variation for a given thickness of the fine-grained layer. All the numerical samples are sheared to 200% shear strain. (a) 1/8 *t* PSZ thickness (b) 1/4 *t* PSZ thickness (c) 3/8 *t* PSZ thickness (d) 1/2 *t* PSZ thickness.
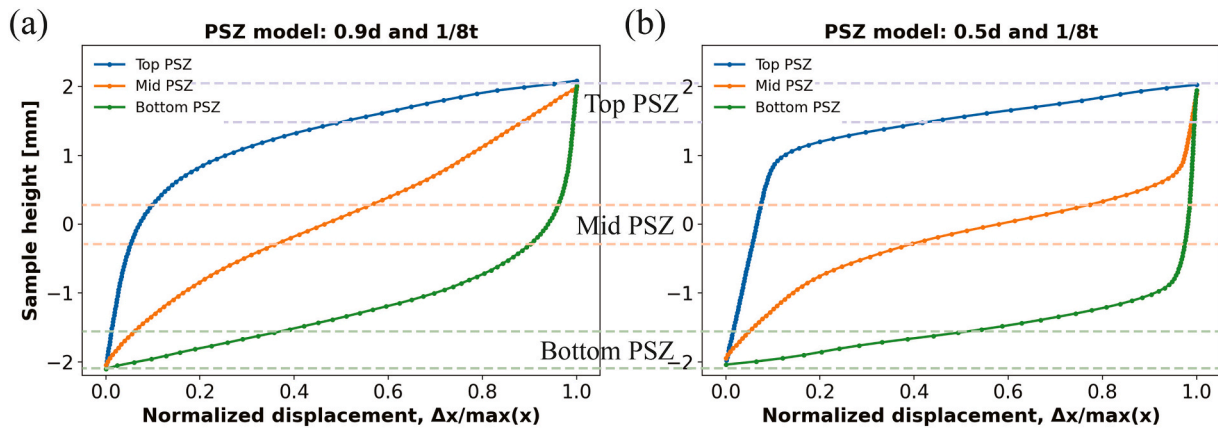
Fig. 5. The comparison between the single-size model, top, middle, and bottom PSZ models with (a) 0.9*d* and 1/8 *t* and (b) 0.5*d* and 1/8 *t*. The dashed lines with the respective color indicate the location of the PSZ.

volume V_σ of a particle can be obtained. Thus, the porosity of each particle can be calculated as $(V_\sigma - V_{particle})/V_\sigma$ (see Catalano et al. (2014) for more detail). In Fig. 8a and b, we show that the deformed fine-grained layer has relatively higher porosity than the deformed coarse-grained layer. For the PSZ thickness contrast of 1/2 *t*, the porosity of the fine-grained layer lies within a range of 0.431 to 0.438. For the PSZ thickness contrast of 1/8 *t*, the porosity of the fine-grained layer is slightly higher (~0.46 to ~0.47) than that using a thickness contrast of 1/2 *t*. The porosity contrast between the fine- and coarse-grained layers is the smallest for the model of 0.9*d*, and slightly increases with increasing contrast in PSZ grain size. We note that there is a significant porosity drop below the FCG interface, suggesting mixing of the fine- and coarse-grained layers. Fig. 8c–d show that the porosity is relatively

constant (around 0.43) across the gouge layer for the model with 0.9*d* whereas porosity increases up to 0.48 only in the fine-grained layers when the contrast in PSZ grain size is down to 0.5. Such observation of the relatively high porosity region is consistent with the slip localization zone (Figs. 4 and 5). This indicates that the fine-grained layer exhibits much more dilatation than the coarse-grained layer during slip and suggest localization of slip within this layer.

3.4. Quantification of slip localization

To quantify the amount of slip localization, we first define the boundary between the spectator and localized regions by determining a critical point (CP) in the displacement curve. Then, the amount of
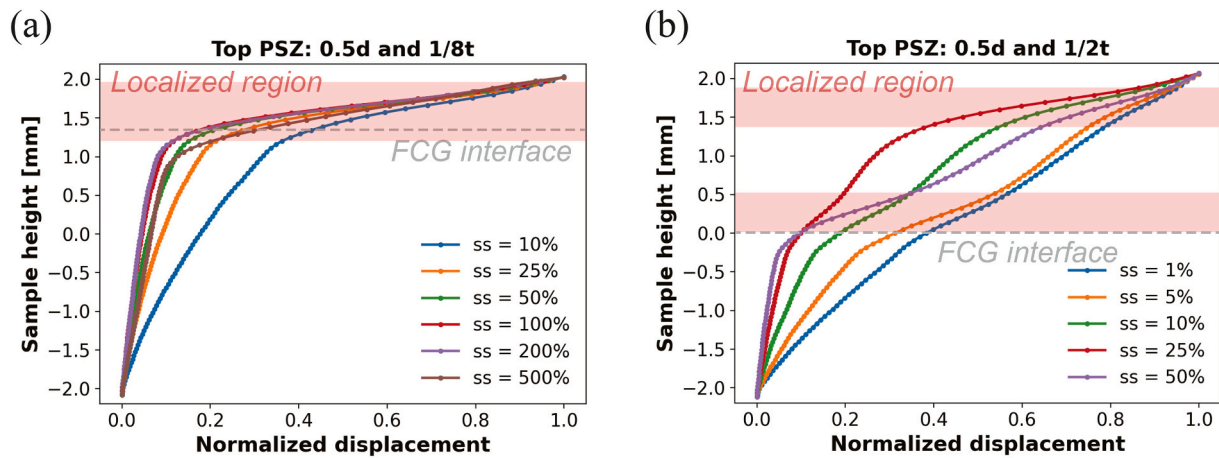
Fig. 6. Normalized particle displacement along the height of sample from 1% to 500% shear strain for (a) the top PSZ model with 0.5*d* and 1/8 *t* and (b) top PSZ model with 0.5*d* and 1/2 *t*.

localization can be calculated by the ratio of the projected length of the localized region on the shear boundary and the total displacement. In most of the PSZ models, we can clearly identify a CP in the displacement curve. However, some simulations show a sign of persistent localization of slip without a distinguishable critical point, such as the PSZ model with 0.9*d* and 1/8 *t* (Fig. 3 and Fig. 5a). To define a CP in those simulations, we apply three different methods: the slope method, the ratio method, and the thickness method. We compare the amount of localization obtained from these methods with each other to infer whether localization exists in those simulations.

In the slope method, we calculate the slope between each adjacent sub-layer of the shear zone and compare the bulk slope pattern with the homogeneous one, as shown in Fig. 9a–b. If the slope between two adjacent sub-layers is larger than that of the homogeneous one, we deduce that this sub-region is potentially a localized region. Based on this information, an intersection point could be found to obtain the critical point. In the ratio method, we calculate the ratio of particle displacement deviation between homogeneous deformation and gouge deformation ($\Delta X = X_{homo} - X_{gouge}$) to homogeneous deformation at each height of the sub-layer. The ratio reflects the degree of slip localization of the entire gouge layer. If the gouge layer is homogeneously deformed, the ratio value is zero across the entire gouge layer, and, in contrast, if there is some localization of slip in the gouge layer, the ratio would be larger than zero. Here, we assume that localization occurs within the gouge layer when the ratio at any sample height is larger than 0.75 or 75%. We choose three different ratios of 0.75, 0.8, and 0.85 as varied PSZ criteria to compare the results with that obtained from the slope method. A critical point is defined as the intersection point between the PSZ criterion and the ratio pattern (Fig. 9c–d). For the middle PSZ model, two intersection points are required to determine the spectator and the localized regions. Note that the region with the ratio larger than 0.75 or 75% determined by the intersection point does not correspond to the location of slip localization. However, the rest of the region with ratio smaller than 0.75 or 75% matches the localization area. The thickness method is only applied to PSZ models where a pre-defined fine-grained layer is used. Instead of determining a critical point, we take the intersection point between the pre-defined FCG interface and the displacement curve as the boundary between the spectator and localized regions. In this method we only quantify the slip within the pre-defined PSZ, and, therefore, we neglect the localization that occurs outside of the PSZ.

In Fig. 9e–f, we show the amount of localization for different locations of PSZ with 0.9*d* and 1/8 *t* sheared to 200% and 500% strain. These models all show a poorly defined CP. The amount of localization of other simulations is summarized in Table S1. We find that over 80% of

localization can be obtained from the slope and ratio methods, irrespectively of shear strain, with the exception of the middle PSZ model which shows particularly low values of 50–60% for localization. For the result obtained from the thickness method, the amount of localization is, in general, 5% to 40% less than that obtained from the slope and ratio method, depending on the location of the PSZ, and its value slightly decreases with the shear strain. This means that (localized) slip is not fully accommodated within the pre-defined PSZ and partial slip occurs within the spectator region, and its contribution increases with accumulating strain.

4. Discussion

4.1. Comparison to previous homogeneous data

We first compare our homogeneous results with Mair and Hazzard (2007) to which our model geometry and the applied particle parameters are comparable. The evolution of the macroscopic friction and the mean friction level of the μ_{qss} for all homogeneous simulations (Fig. S2) is consistent with previous laboratory experimental and 3-D numerical data (Mair et al., 2002; Hazzard and Mair, 2003; Mair and Hazzard, 2007). A notable difference is that, in all the homogeneous models, a peak in friction appears at initial shearing stages, accompanied by an increase in gouge dilation, and variable amounts of displacement-dependent weakening can be observed for the models with different PSDs. The deformation patterns of the gouge layer are also comparable. Fig. 10 shows the comparison of the gouge deformation pattern between ours and Mair and Hazzard (2007). In Mair and Hazzard (2007), the gouge deformation in both the Gaussian PSD (green curve) and *D* of 2.6 (purple curve) also reveal a degree curvature non-linearity, which suggests that the shear rate across the interface is non-linear. Although their results do not show deviation from a narrow to wide PSD as much as ours (orange and red curves), which might be owing to lower shear strain rate (lower inertial number) or other factors like the applied timestep, the comparison of the results demonstrates that the numerical results obtained in our study is accurate and reliable. In fact, the evolution of the pattern of gouge deformation from localized deformation to homogeneous deformation with increasing PSD is more systematic in our study. Such a transition may be associated with the number of fine grains in the granular packing that facilitate homogeneous shearing. However, the underlying mechanisms remains unclear and is out of the scope of the current study.

(a)

(b)

(c)
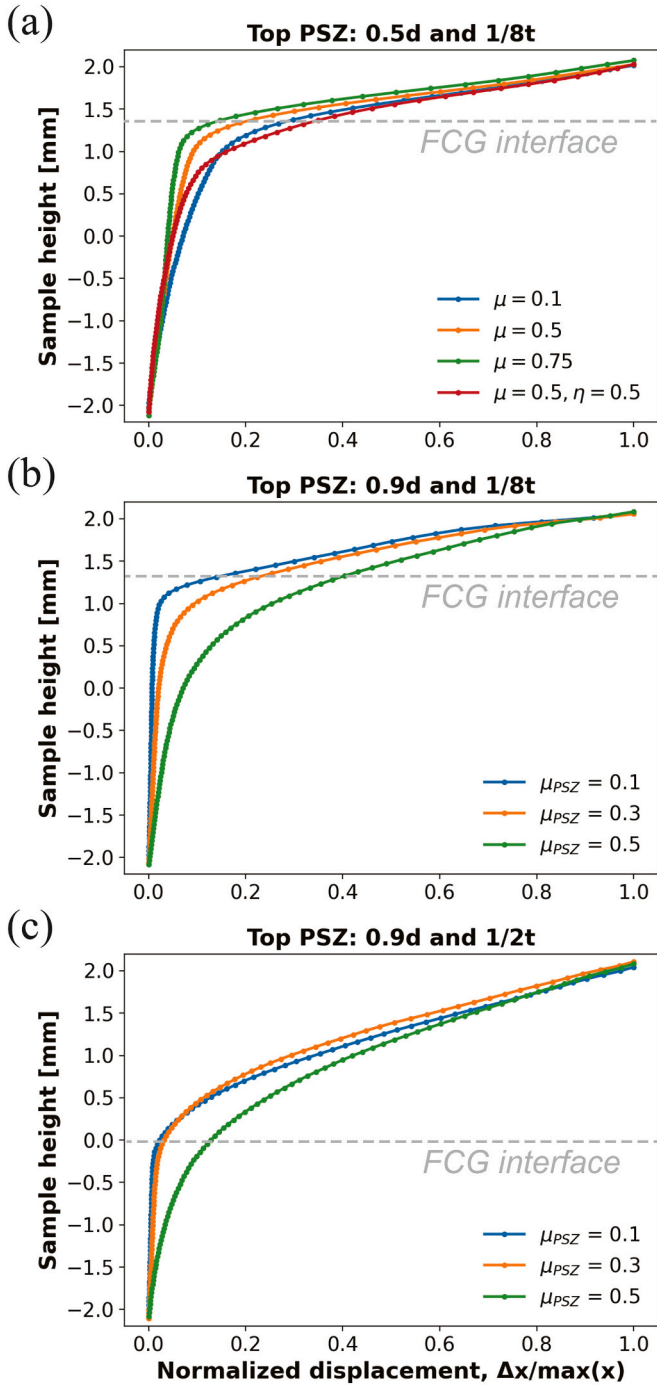
Fig. 7. Sample height as a function of normalized particle displacement for numerical models using different values for μ (0.1, 0.5, and 0.75) and η (0, 0.5). (a) Top PSZ model with 0.5d and 1/8 t; (b, c) Top PSZ models (0.9d and 1/8 t as well as 0.9d and 1/2 t) with varied μ_{PSZ} (0.1, 0.3, 0.5).

4.2. The PSZ model

4.2.1. Evolution of macroscopic friction and volumetric behavior

The evolution of the macroscopic friction and the mean friction level of the μ_{qss} for all PSZ simulations is comparable to the homogeneous simulations. An imposed fined-grained layer, independent of its thickness and grain size, does not show to have an influence on the mechanical response. This is different from previous laboratory experimental observations where a weakening behavior (i.e., stress drop from a peak to steady-state friction) is usually observed to be

accompanied by the generation of a principal slip zone (e.g., Smith et al., 2015). Such a difference can be explained by the absence of grain comminution processes and frictional heating at grain contacts in the current numerical simulation.

4.2.2. Granular deformation

The previous 2-D and 3-D numerical studies have shown that persistent localized deformation is hardly observed in a homogeneous granular layer under low single shearing velocities (i.e., V < 1 μm/s, for example in Morgan and Boettcher, 1999; Mair and Hazzard, 2007) or seismic velocity-stepping simulations (i.e., 10^{-3} < V < 10^{0} m/s; Ferdowsi and Rubin, 2020) when processes like grain breakage (e.g., Mair and Abe, 2008; Abe and Mair, 2009), time-dependent healing (e.g., Morgan, 2004), cohesion of grain contacts (e.g., Casas et al., 2022), or fluid overpressurization (e.g., Nguyen et al., 2021) are not included in models. In our homogeneous model, we also do not observe persistent localization in the granular packing in the Gaussian PSD and power-law PSD models, except for the single-size and narrow Gaussian PSD models where we find that the slip is accommodated preferentially in the top about 1.2 mm of the gouge layer after 200% shear strain (Fig. S3). after 200% shear strain (Fig. S3). These non-liner displacement curves were also observed in Mair and Hazzard (2007). Note that we used nearly the same model configuration and particle parameters as their model. However, our results show a more systematic evolution of deformation from a 'localized' pattern to a homogeneous pattern with increasing particle size distribution. Such a transition may be associated with the number of fine grains in the granular packing that facilitate homogeneous shearing.

In the PSZ models, we observe persistent localized deformation in the gouge layer where, regardless of which quantification methods we use, most models show >75% of slip is localized, with the exception of the middle PSZ model with a grain size contrast of 0.9 and a thickness of 1/8 that shows a particularly low amount (~20%; Fig. 8f). Although the amount of localization varies slightly using different methods of quantification, all values progressively increase with increasing contrast in grain size and PSZ thickness, indicating that the amount of localization is highly sensitive to the grain size and the thickness of the fine-grained layer.

4.2.3. FCG interface

A major question is how and why shear localizes in the layer of smaller grains in the absence of any time-dependent grain-contact mechanism. In Fig. 4d, we show that the amount of localization increases with increasing grain size contrast for a PSZ model with the thickness contrast of 0.5 t. With this thickness contrast, we can observe that over 90% of slip is localized within the fine-grained layer when the contrast in grain size is >25%. However, the localized patterns in the fine-grained layer vary between different grain size contrasts, which transforms from a nearly straight line with 0.75d to a curve-shaped line with 0.5d. This observation indicates that more slip is accommodated close to the FCG interface even though the strain is nearly fully localized within the fine-grained layer. In addition, the phenomenon suggests that the initial slip occurs at the boundary, i.e., at the FCG interface. This is consistent with the model configuration we applied for the initial packing conditions of the fine-grained and coarse-grained layers. Both layers should possess identical porosity, average coordination number of each particle, contact force network (i.e., pipe-like network) due to the use of singe-size PSD within each layer. The main difference might be that the total contact force at grain contacts of the fine-grained layer is lower compared to coarse-grained layer (Fig. 11) due to the decrease in the contact radius and thus the contact stiffness. However, the total grain contact area for both layers should remain identical as the number of grain contacts in the fine-grained layer also significantly increases. Therefore, it is complicated to explain why localization occurs within a layer of smaller grain sizes. However, properties at the FCG interface are significantly different. At the FCG interface before shearing, the mixture
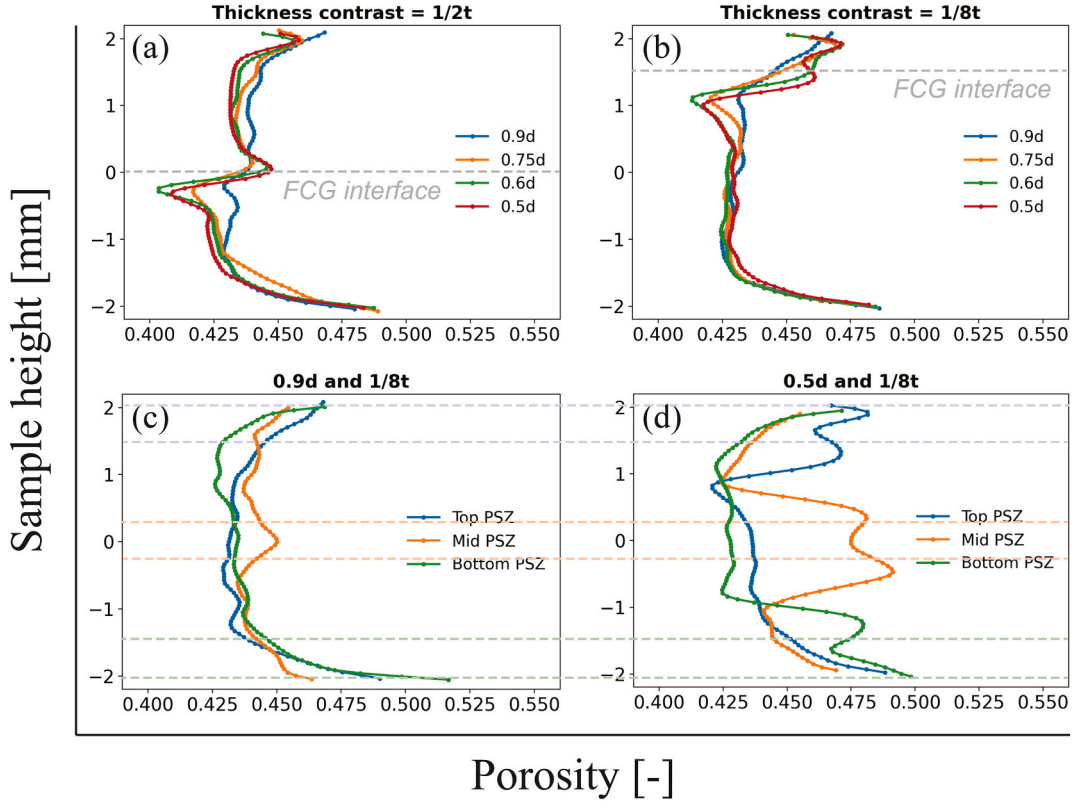
Fig. 8. Assemblage porosity along the sample height for numerical models with different PSZ thicknesses and grain sizes as well as the location of the PSZ. (a) 1/2 *t* PSZ thickness (b) 1/8 *t* PSZ thickness (c) 0.9*d* PSZ grain size and 1/8 *t* PSZ thickness (d) 0.5*d* PSZ grain size and 1/8 *t* PSZ thickness.

of fine and coarse grains provides a lower porosity and an increase in average coordination number of large grains. The interface region also becomes a contrast boundary in terms of grain size, contact stiffness, and contact force. It is very likely that the above factors trigger the initial slip at the grain contacts at the interface; however, the controlling role of each variable remains unclear.

To explore the localization of strain within the fine-grained layer after that the slip initiates at the boundary, we apply the concept of the average spreading velocity parameter V_k^v and the squeeze expulsion theory parameter T_k^v (e.g., Jing et al., 2017; Lai et al., 2017) to investigate the kinematic differences in a layer with different sized particles and the developed force imbalances when particles are squeezed between each other. The V_k^v and T_k^v are defined as:

$$V_k^v = \frac{1}{N_k} \sum_{i=1}^{N_k} V_i^v \tag{16}$$

$$T_k^v = \frac{1}{N_k} \sum_{i=1}^{N_k} \frac{F_i^v}{\rho \pi r^3} \tag{17}$$

Where V_i^γ is the vertical velocity of particle i, N_k is the number of the d-size particles for the fine- and coarse-grained layer, F_i^γ is the vertical resultant force of particle i via particle interactions, ρ is the grain density, and r is the grain radius. The V_i^γ and F_i^γ of particles only considers the direction away from the FCG interface to evaluate the contribution of particle interactions to the fine and coarse grains. For example, if the fine-grained layer is on top of the coarse-grained layer (i.e., most of the scenarios in this study), we adopt the positive and negative value for both V_i^γ and F_i^γ for the fine- and coarse-grained layers, respectively. The larger values of V_k^γ indicate more enhanced granular flow mobility and the collision dominant flow pattern, and the larger values of T_k^γ indicates more contributions of particle interactions to accelerate the spread of particles.

Fig. 12 shows the evolution of V_k^γ and T_k^γ as a function of shear strain

of 1% to 50% for the fine- and coarse-grained layers. We find that the coarse-grained layer initially possesses relatively large V_k^γ of ~0.026 m/s and T_k^γ of ~220.5 m/s^2 at the shear strain of 1% without visible persistent slip localization. As shear strain increases up to 5%, we observe a significant drop for both V_k^γ and T_k^γ for the coarse-grained layer accompanied by a sharp increase in the fine-grained layer. The differences in the values of V_k^γ and T_k^γ between the fine- and coarse-grained layers do not vary with further shear strain and the localization process carries on. The combined results suggest that the phenomenon of slip localization is associated with the kinematic difference and the force imbalance between the fine- and coarse-grained layers. Initially, larger contributions of particle interactions happen within the coarse-grained layer than the fine-grained layer which is likely due to the particle mass variation. Shortly, with progressively slip, the fine grains become more vigorous and can slip more than the coarse grains because smaller grains acquire more spreading velocity when in contact with a large grain. This concept is similar to the momentum transfer where most of the momentum of the coarse-grained layer is transferred to the fine-grained layer. We suggest that the contrast in the stiffness and contact force causes initial slip on the boundary, and the fine-grained layer is prone to slip and dilate owing to the transition of the contributions of the particle interactions from the coarse-grained layer.

4.2.4. Effect of interparticle friction on slip localization

According to Morgan (1999), for the same contact force, sliding between particles will be activated more easily in a low *μ* system than in a high *μ* system because of the low assigned critical force. On the other hand, interparticle rolling will become more active if *μ* is sufficiently high to inhibit sliding to occur. Based on the results of the different *μ* systems, we show that the slip becomes more localized within the fine-grained layer with increasing *μ* for the entire system (Fig. 7). This suggests that interparticle rolling is the main mechanism that accommodates slip as we have shown that particles are easier to dilate within the
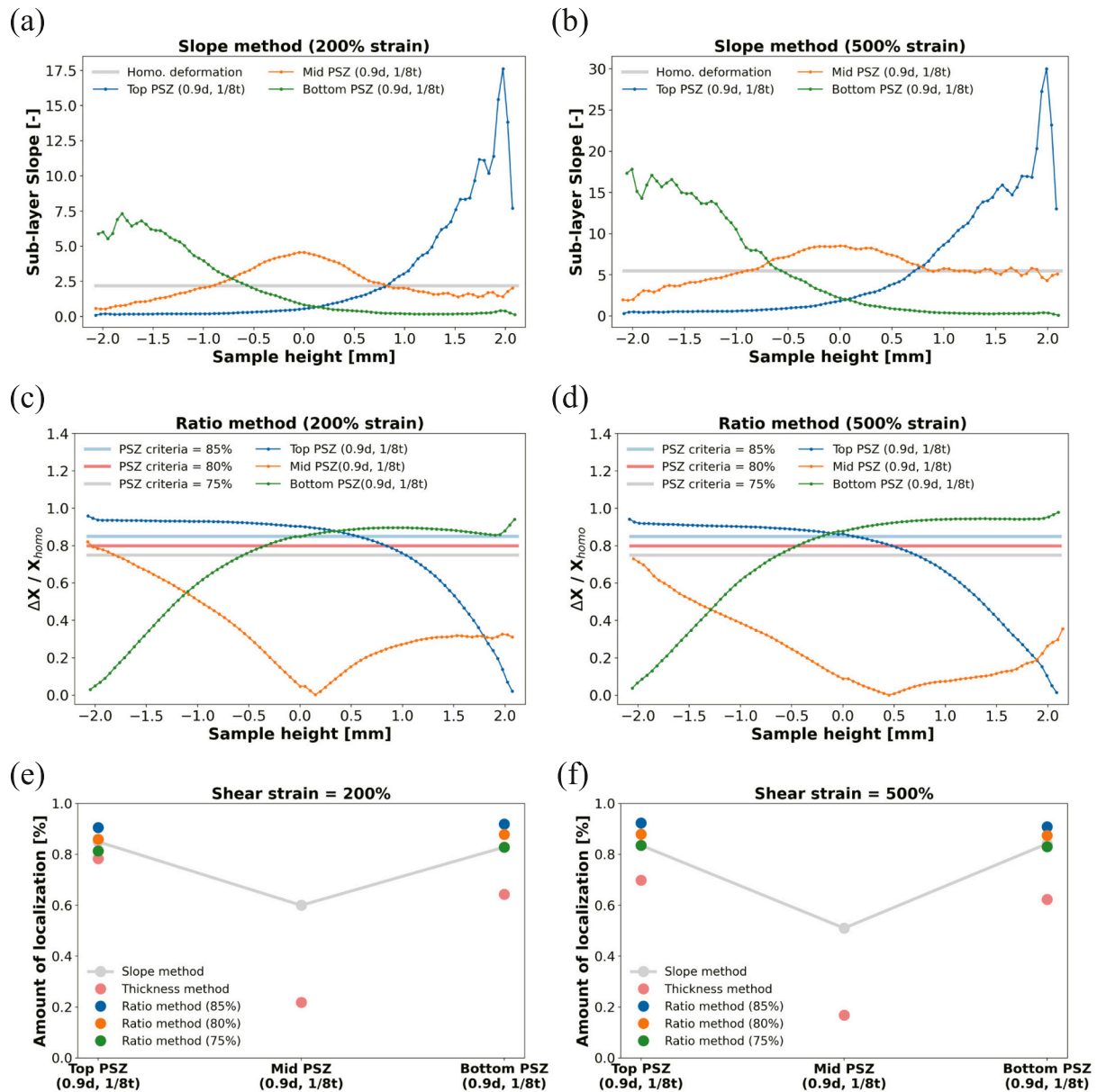
Fig. 9. The slope and ratio methods together with the quantification of slip localization for the top PSZ, middle PSZ, and bottom PSZ models at shear strain of 200% and 500%. (a, b) The slope method; (c, d) The ratio method; (e, f) The obtained amount of localization from the three methods for different simulations.

fine-grained layer during shearing. In addition, we show the profile of the angular velocity distribution for each particle for the single-size and PSZ model with 0.5d and 1/8 t fine-grained layer at the top, middle, and bottom of the granular layer at 200% shear strain (Fig. 13). Large angular velocity of particles is observed specifically in the fine-grained layer, indicating that slip is accommodated largely by interparticle rolling, which is consistent with the result of the PSZ model with different μ (Fig. 7a), showing that the high μ assemblage (system favored to interparticle rolling) provides the largest degree of localization. The volumetric strain data also supports the observation where the granular layer with high μ exhibits the largest amount of dilation whereas the one with low μ exhibits mostly compaction (see Fig. S4). Since high μ inhibits interparticle sliding and promotes interparticle rolling (also the dilation angle between particles), the granular layer would dilate more than the one dominated by the interparticle sliding.

However, if we only reduce the μ of the fine-grained layer to a lower value (0.1 and 0.3) instead of the entire granular assemblage (Fig. 7b and c), the degree of localization still increases. Such difference is likely

to be due to the variation of contact normal and shear forces between the fine- and coarse-grained layers. Even in a high μ granular assemblage, interparticle sliding might still be very likely to occur within the fine-grained layer due to the low contact force. On the other hand, the decrease in μ for the entire system does not necessarily facilitate localization. Altogether, our results also suggest that the increasing percentage of interparticle sliding can facilitate slip localization.

4.3. Comparison with laboratory results and implications

Numerous laboratory experiments performed on room-dry and wet gouges at high slip velocity (i.e., > 0.1 m/s) have reported that slip tends to be localized at the boundary of the gouge layer, forming a so-called PSZ (Smith et al., 2015; Kuo et al., 2014; Boulton et al., 2017; Yao et al., 2018; Hunfeld et al., 2021). Smith et al. (2015) reported that the formation of a PSZ through grain fragmentation is a critical precursor to dynamic weakening in calcite gouges which is associated with thermal-induced mechanisms like flash heating and weakening. In addition, he
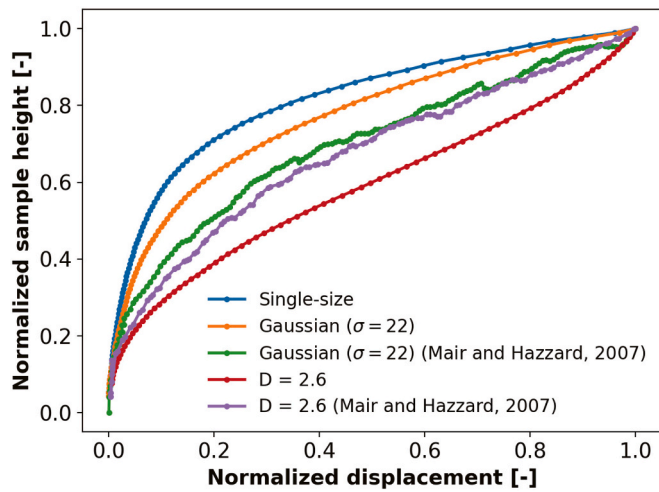
Fig. 10. Comparison of the gouge deformation pattern between our homogeneous shear model and Mair and Hazzard (2007). Note that the imposed shear strain is 200% and 100% in our and Mair and Hazzard (2007), respectively.

reported different types of shear localized features which developed at different frictional stages, in which R-shear is intially developed at around peak stress followed by Y- or boundary shears at steady-state.

However, our results do not show a clear link between the development of the localization and different frictional stages which might be due to the method of analyzing the localization.

On the other hand, without thermal-induced mechanisms, Reches and Lockner (2010) inferred that dynamic gouge formation is an effective lubrication mechanism to reduce fault strength. Han et al. (2010) also reported that the presence of nanoparticles in a fault zone can be an important lubrication processes due to nanoparticle rolling. However, according to our PSZ models, the presence of the fine-grained layer does not necessarily reduce the shear strength and the bulk macroscopic friction only decreases when the fine-grained layer has lower interparticle friction (which also promotes particle sliding rather rolling). Thus, frictional-induced heating mechanisms such as flash heating or thermal pressurization at grain contacts are required for dynamic weakening (see also Yao et al., 2016).

Previous low- and high-velocity friction experiments reported that slip tends to be accommodated within the PSZ once a fine-grained layer has formed due to grain size reduction (Ikari, 2015; Smith et al., 2015). As grain size reduction may induce rounding of particles, according to our numerical results (Fig. 7e), less slip may be accommodated within the PSZ instead due to the increasing importance of interparticle rolling within the fine-grained layer. Such contradictory observation may suggest that only the rounding effect on particles due to grain-to-grain comminution is not sufficient for further localization of slip within a PSZ. This suggests that in the absence of thermal weakening mechanisms
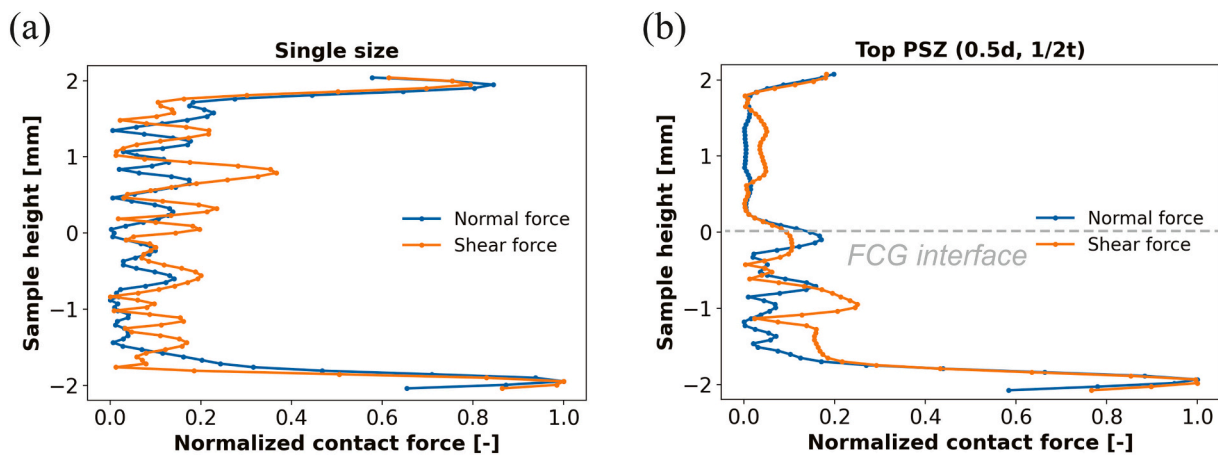
Fig. 11. The normalized contact forces (both normal and shear forces) along the sample height for (a) the single-size model, and (b) the top PSZ model (0.5d, 1/2 t) at 200% shear strain.
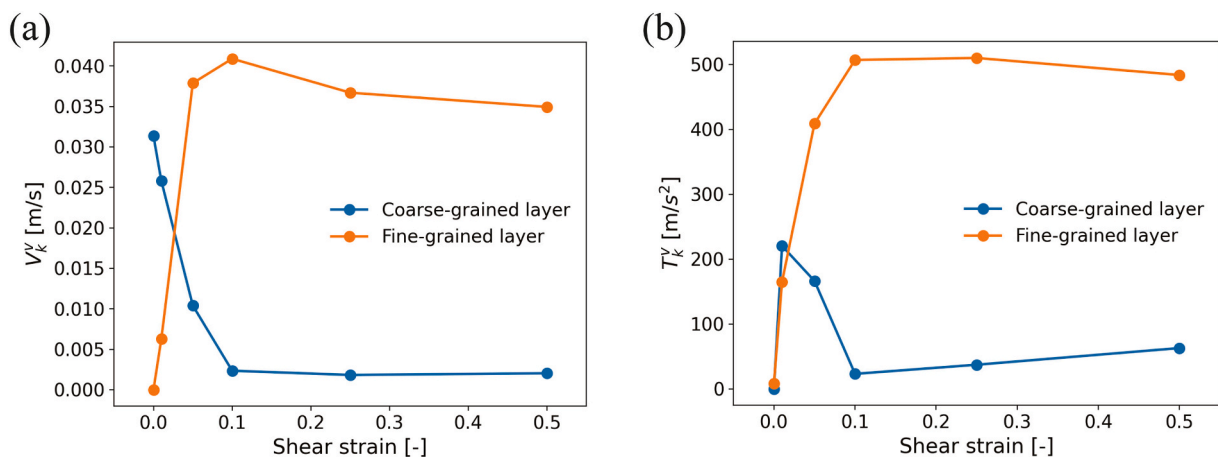
Fig. 12. (a) average spreading velocity parameter V_k^v and (b) mechanical parameter T_k^v as a function of shear strain (1%, 5%, 10%, 25%, and 50%) for the fine- and coarse-grained layers. An example of the top PSZ model with 0.5d and 0.5 t.
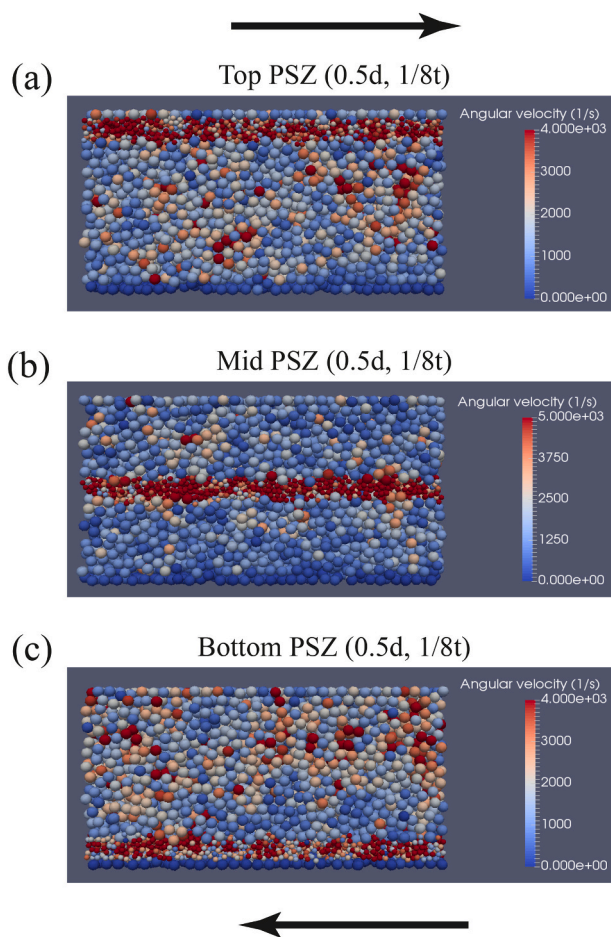
Fig. 13. Distribution of angular velocity in the shear direction (*x*-direction) of each particle after 200% shear strain for the models with (a) a single-size PSD; (b) a top PSZ; (c) a middle PSZ; (d) a bottom PSZ all with 0.5*d* and 1/8 *t* of the granular assemblage. The warm color indicates high angular velocity while the cool color indicates low angular velocity.

within the PSZ, the layer with fine-grained particles (PSZ) will continue to grow during shear due to grain size reduction, resulting from slip occurring outside of the PSZ.

5. Conclusions

We use 3-D DEM simulations to investigate strain localization in a non-destructive granular layer under seismic slip velocities. We build a direct shear model with a distinct configuration, a principal slip zone (PSZ) model with variation in grain size and thickness between the single-size fine- and coarse-grained layer. In addition, a series of particle parameters and values are used to investigate their effect on slip localization. The conclusions are summarized as below:

(1) For an assemblage with a pre-defined fine-grained layer, we show that slip is prone to be localized within the fine-grained layer and the amount of localization is sensitive to the relative grain size and layer thickness of the PSZ.

(2) We reveal that slip is prone to be largely accumulated near the grain-size contrast boundary. This is likely due to the fact that the boundary represents a significant contrast in the contact stiffness and contact force between the fine- and coarse-grained layers. The applied concept of spreading velocity and squeeze expulsion theory provides a plausible explanation for slip localization as

smaller grains acquire more kinematic energy when large grains bump into them.

(3) By comparison with natural and laboratory observations, we conclude that the presence of a weaker, fine-grained layer within a dense fault zone is likely to result in self-enhanced weakening of the fault planes. In addition, thermal mechanisms at grain-to-grain contacts (i.e., flash heating and weakening) are needed to induce dynamic weakening of a fault.

CRediT authorship contribution statement

Chien-Cheng Hung: Conceptualization, Data curation, Formal analysis, Investigation, Methodology, Resources, Validation, Visualization, Writing – original draft. **André R. Niemeijer:** Conceptualization, Project administration, Supervision, Writing – review & editing. **Amir Raoof:** Methodology, Software, Supervision, Writing – review & editing. **Thomas Sweijen:** Conceptualization, Methodology, Software, Validation, Visualization, Writing – review & editing.

Declaration of Competing Interest

The authors declare that they have no known competing financial interests or personal relationships that could have appeared to influence the work reported in this paper.

Data availability

Data will be made available on request.

Appendix A. Supplementary data

Supplementary data to this article can be found online at https://doi.org/10.1016/j.tecto.2023.229974.

References

Abe, S., Mair, K., 2009. Effects of gouge fragment shape on fault friction: new 3D modelling results. Geophys. Res. Lett. 36 (23).
Boullier, A.M., 2011. Fault-zone geology: lessons from drilling through the Nojima and Chelungpu faults. Geol. Soc. Lond., Spec. Publ. 359 (1), 17–37.
Boullier, A.M., Yeh, E.C., Boutareaud, S., Song, S.R., Tsai, C.H., 2009. Microscale anatomy of the 1999 Chi-Chi earthquake fault zone. Geochem. Geophys. Geosyst. 10 (3).
Boulton, C., Yao, L., Faulkner, D.R., Townend, J., Toy, V.G., Sutherland, R., Shimamoto, T., 2017. High-velocity frictional properties of Alpine Fault rocks: mechanical data, microstructural analysis, and implications for rupture propagation. J. Struct. Geol. 97, 71–92.
Casas, N., Mollon, G., Daouadji, A., 2022. DEM analyses of cemented granular fault gouges at the onset of seismic sliding: peak strength, development of shear zones and kinematics. Pure Appl. Geophys. 179 (2), 679–707.
Catalano, E., Chareyre, B., Barthélémy, E., 2014. Pore-scale modeling of fluid-particles interaction and emerging poromechanical effects. Int. J. Numer. Anal. Methods Geomech. 38 (1), 51–71. https://doi.org/10.1002/nag.2198.
Chester, F.M., Chester, J.S., 1998. Ultracataclasite structure and friction processes of the Punchbowl fault, San Andreas system, California. Tectonophysics 295 (1–2), 199–221.
Chester, F.M., Evans, J.P., Biegel, R.L., 1993. Internal structure and weakening mechanisms of the San Andreas fault. J. Geophys. Res. Solid Earth 98 (B1), 771–786.
De Paola, N., Collettini, C., Faulkner, D.R., Trippetta, F., 2008. Fault zone architecture and deformation processes within evaporitic rocks in the upper crust. Tectonics 27 (4).
De Paola, N., Hirose, T., Mitchell, T., Di Toro, G., Viti, C., Shimamoto, T., 2011. Fault lubrication and earthquake propagation in thermally unstable rocks. Geology 39 (1), 35–38.
Ferdowsi, B., Rubin, A.M., 2020. A granular physics-based view of fault friction experiments. J. Geophys. Res. Solid Earth 125 (6) e2019JB019016.
Fondriest, M., Smith, S.A., Di Toro, G., Zampieri, D., Mittempergher, S., 2012. Fault zone structure and seismic slip localization in dolostones, an example from the Southern Alps, Italy. J. Struct. Geol. 45, 52–67.
Fondriest, M., Smith, S.A., Candela, T., Nielsen, S.B., Mair, K., Di Toro, G., 2013. Mirror-like faults and power dissipation during earthquakes. Geology 41 (11), 1175–1178.
Han, R., Hirose, T., Shimamoto, T., 2010. Strong velocity weakening and powder lubrication of simulated carbonate faults at seismic slip rates. J. Geophys. Res. Solid Earth 115 (B3).

Hazzard, J.F., Mair, K., 2003. The importance of the third dimension in granular shear. Geophys. Res. Lett. 30 (13).

Heermance, R.V., Chen, J., Burbank, D.W., Miao, J., 2008. Temporal constraints and pulsed Late Cenozoic deformation during the structural disruption of the active Kashi foreland, northwest China. Tectonics 27 (6).

Heesakkers, V., Murphy, S., Reches, Z., 2011. Earthquake rupture at focal depth, part I: structure and rupture of the Pretorius fault, TauTona mine, South Africa. Pure Appl. Geophys. 168 (12), 2395–2425.

Hunfeld, L.B., Niemeijer, A.R., Spiers, C.J., 2017. Frictional properties of simulated fault gouges from the seismogenic groningen gas field under in situ P–T-chemical conditions. J. Geophys. Res. Solid Earth 122 (11), 8969–8989.

Hunfeld, L.B., Chen, J., Niemeijer, A.R., Ma, S., Spiers, C.J., 2021. Seismic slip-pulse experiments simulate induced earthquake rupture in the Groningen gas field. Geophys. Res. Lett. 48 (11) e2021GL092417.

Ikari, M.J., 2015. Principal slip zones: precursors but not recorders of earthquake slip. Geology 43 (11), 955–958.

Itasca, C., 1999. PFC 3D-User Manual. Itasca Consulting Group, Minneapolis, p. 435.

Iwashita, K., Oda, M., 1998. Rolling resistance at contacts in simulation of shear band development by DEM. J. Eng. Mech. 124 (3), 285–292.

Jing, L., Kwok, C.Y., Leung, Y.F., 2017. Micromechanical origin of particle size segregation. Phys. Rev. Lett. 118 (11), 118001.

Kitajima, H., Chester, J.S., Chester, F.M., Shimamoto, T., 2010. High-speed friction of disaggregated ultracataclasite in rotary shear: characterization of frictional heating, mechanical behavior, and microstructure evolution. J. Geophys. Res. Solid Earth 115 (B8).

Kuo, L.W., Li, H., Smith, S.A., Di Toro, G., Suppe, J., Song, S.R., Si, J., 2014. Gouge graphitization and dynamic fault weakening during the 2008 Mw 7.9 Wenchuan earthquake. Geology 42 (1), 47–50.

Lai, Z., Vallejo, L.E., Zhou, W., Ma, G., Espitia, J.M., Caicedo, B., Chang, X., 2017. Collapse of granular columns with fractal particle size distribution: implications for understanding the role of small particles in granular flows. Geophys. Res. Lett. 44 (24), 12–181.

Logan, J.M., Dengo, C.A., Higgs, N.G., Wang, Z.Z., 1992. Fabrics of experimental fault zones: their development and relationship to mechanical behavior. In: International Geophysics, vol. 51. Academic Press, pp. 33–67.

Ma, G., Zou, Y., Gao, K., Zhao, J., Zhou, W., 2020. Size polydispersity tunes slip avalanches of granular gouge. Geophys. Res. Lett. 47 (23) e2020GL090458.

Mair, K., Abe, S., 2008. 3D numerical simulations of fault gouge evolution during shear: grain size reduction and strain localization. Earth Planet. Sci. Lett. 274 (1–2), 72–81. https://doi.org/10.1016/j.epsl.2008.07.010.

Mair, K., Hazzard, J.F., 2007. Nature of stress accommodation in sheared granular material: Insights from 3D numerical modeling. Earth Planet. Sci. Lett. 259 (3), 469–485. https://doi.org/10.1016/j.epsl.2007.05.006.

Mair, K., Frye, K.M., Marone, C., 2002. Influence of grain characteristics on the friction of granular shear zones. J. Geophys. Res. Solid Earth 107 (B10), ECV 4–9. https://doi.org/10.1029/2001JB000516.

Mindlin, R.D., 1949. Compliance of Elastic Bodies in Contact.

Modenese, C., 2013. Numerical Study of the Mechanical Properties of Lunar Soil by the Discrete Element Method. Doctoral dissertation. Oxford University, UK.

Morgan, J.K., 1999. Numerical simulations of granular shear zones using the distinct element method: 2. Effects of particle size distribution and interparticle friction on mechanical behavior. J. Geophys. Res. Solid Earth 104 (B2), 2721–2732.

Morgan, J.K., 2004. Particle dynamics simulations of rate- and state-dependent frictional sliding of granular fault gouge. Pure Appl. Geophys. 161 (9), 1877–1891. https://doi.org/10.1007/s00024-004-2537-y.

Morgan, J.K., Boettcher, M.S., 1999. Numerical simulations of granular shear zones using the distinct element method: 1. Shear zone kinematics and the micromechanics of localization. J. Geophys. Res. Solid Earth 104 (B2), 2703–2719.

Nguyen, H.N.G., Scholtès, L., Guglielmi, Y., Donzé, F.V., Ouraga, Z., Souley, M., 2021. Micromechanics of sheared granular layers activated by fluid pressurization. Geophys. Res. Lett. 48 (14) e2021GL093222.

Platt, J.D., Brantut, N., Rice, J.R., 2015. Strain localization driven by thermal decomposition during seismic shear. J. Geophys. Res. Solid Earth 120 (6), 4405–4433.

Reches, Z.E., Lockner, D.A., 2010. Fault weakening and earthquake instability by powder lubrication. Nature 467 (7314), 452–455.

Šmilauer, V., Catalano, E., Chareyre, B., Dorofeenko, S., Duriez, J., Gladky, A., Thoeni, K., 2010. Yade reference documentation. Yade Documentation 474 (1).

Smith, S.A., Billi, A., Toro, G.D., Spiess, R., 2011. Principal slip zones in limestone: microstructural characterization and implications for the seismic cycle (Tre Monti Fault, Central Apennines, Italy). Pure Appl. Geophys. 168 (12), 2365–2393.

Smith, S.A.F., Di Toro, G., Kim, S., Ree, J.H., Nielsen, S., Billi, A., Spiess, R., 2013. Coseismic recrystallization during shallow earthquake slip. Geology 41 (1), 63–66.

Smith, S.A., Nielsen, S., Di Toro, G., 2015. Strain localization and the onset of dynamic weakening in calcite fault gouge. Earth Planet. Sci. Lett. 413, 25–36.

Thornton, C., Cummins, S.J., Cleary, P.W., 2011. An investigation of the comparative behaviour of alternative contact force models during elastic collisions. Powder Technol. 210 (3), 189–197.

Yao, L., Shimamoto, T., Ma, S., Han, R., Mizoguchi, K., 2013. Rapid postseismic strength recovery of Pingxi fault gouge from the Longmenshan fault system: experiments and implications for the mechanisms of high-velocity weakening of faults. J. Geophys. Res. Solid Earth 118 (8), 4547–4563.

Yao, L., Ma, S., Niemeijer, A.R., Shimamoto, T., Platt, J.D., 2016. Is frictional heating needed to cause dramatic weakening of nanoparticle gouge during seismic slip? Insights from friction experiments with variable thermal evolutions. Geophys. Res. Lett. 43 (13), 6852–6860.

Yao, L., Ma, S., Chen, J., Shimamoto, T., He, H., 2018. Flash heating and local fluid pressurization lead to rapid weakening in water-saturated fault gouges. J. Geophys. Res. Solid Earth 123 (10), 9084–9100.

Zhu, H., Zhou, W.H., Yin, Z.Y., 2018. Deformation mechanism of strain localization in 2D numerical interface tests. Acta Geotech. 13 (3), 557–573.